PHYSICAL REVIEW A VOLUME 32, NUMBER 3 SEPTEMBER 1985

Associative ionization mechanisms in collisions between He($5\,^3P$) and He(1^1S) atoms at thermal energies

S. Runge,* A. Pesnelle, M. Perdrix, and G. Watel
Service de Physique des Atomes et des Surfaces, Centre d'Etudes Nucléaires de Saclay, 91191 Gif-sur-Yvette Cédex, France

J. S. Cohen
Theoretical Division, Los Alamos National Laboratory, University of California, Los Alamos, New Mexico 87544

(Received 18 March 1985)

Homonuclear associative ionization, also known as the Hornbeck-Molnar process, has been investigated in a crossed-beam experiment for the collision He(5^3P)+He with use of a time-of-flight technique. Excited states were produced from metastable He(2^3S) with use of a tunable cw source of coherent light. The density distribution of the He(5^3P) atoms in the interaction zone was investigated by a highly sensitive photoionization method. The combination of these techniques with a crossed-beam geometry allowed the kinetic-energy dependence of the cross section to be investigated with a very good resolution in the range 20—200 meV. The experimental curve exhibits structures similar to that calculated by Cohen for the excited states 3^3P and 4^3P. The interpretation of our results has been performed by an extension of Cohen's model to the present case, considering bound-bound transitions between quasidiabatic states of He_2^*, and assuming a 100% ionization rate for the states penetrating into the continuum. The shape of the experimental curve is well reproduced by the contribution due to channels of $^3\Pi_u$ symmetry, which is found to be preponderant, and the validity of Cohen's model is thus demonstrated. Two different processes are found to occur in different regions of the kinetic-energy range separated by a narrow transition zone. The limits of the latter are the diabatic threshold [crossing energy of the repulsive entrance channel $^3\Pi_u$ 5^3P with the ionization limit $He_2{}^+(X^2\Sigma_u^+)$], and the asymptotic energy of the first attractive channel $^3\Pi_u$ 6^3D.

I. INTRODUCTION

The fundamental processes arising in noble-gas discharges have been studied for many years. In thermal collisions between two identical atoms, one of them being in an excited state (denoted by A^*), two kinds of inelastic reactions may occur. The first one is homonuclear associative ionization,

$$A^* + A \rightarrow A_2{}^+ + e^- , \tag{1}$$

and the second is nonresonant excitation transfer,

$$A^*(nLSJ) + A \rightarrow A^*(n'L'S'J') + A . \tag{2}$$

The former process was first identified by Hornbeck and Molnar in 1951 (Ref. 1) and is often referred to by the names of these authors. The study of Hornbeck-Molnar ionization (HMI) is of fundamental interest as a test of ionizing collision theory and has strong implications in astrophysics and plasma physics. In particular, it is certainly involved in the optogalvanic effect.[2]

The existence of a similar process in the alkali metals has been observed since 1923.[3,4] Homonuclear associative ionization contributes to the bulk process in the ionization of an alkali-metal vapor irradiated by resonant light,[5–7] and its interpretation is related to that of HMI.

For a long time, it has only been possible to experimentally determine appearance potentials for molecular ions in noble-gas discharges.[4] In our group we have obtained a rigorous upper limit for this parameter in helium, corresponding to the collision He(3^1P)+He.[8] Since the pioneering work of Wellenstein and Robertson,[9] very few experimental studies have been devoted to measurements of such reaction cross sections. These authors obtained cross-section values, averaged over the velocity distributions of the colliding atoms at 340 K, in the range $(1.6\text{—}20)\times 10^{-16}$ cm^2 for the systems He($3^{1,3}P$)+He, and He($3^{1,3}D$)+He.

The system He(5^3P)+He was studied by Collins *et al.*,[10] who obtained a rate coefficient of 8×10^{-11} cm^3 s^{-1} from an analysis of the quenching rate of He(5^3P) in an afterglow. Assuming a thermal velocity distribution at 300 K, this leads to an average HMI cross section of about 5×10^{-16} cm^2, in good agreement with the results of Wellenstein and Robertson. Until recently, other experimental investigations have been carried out on the quenching rates of excited helium states in discharges,[11–13] leading to cross sections or reaction rates averaged over thermal velocity distributions. The aim of the present work is to determine the mechanisms responsible for the HMI in the presence of helium atoms, using a crossed-beam experiment to obtain the energy dependence of the cross section.

A characteristic feature of the HMI is that the potential energy of the system at the separated atom limit is lower in the incoming channel than in the outgoing channel (see Fig. 1). A similar situation is sometimes encountered in heteronuclear systems, such as N(^2D)+O, which has been

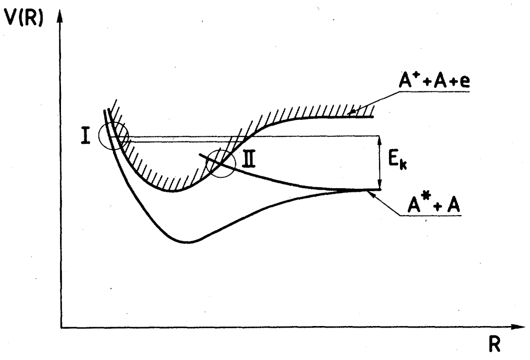

FIG. 1. Typical potential curves illustrating the different theoretical approaches for HMI. Region I: vibronic coupling involving an adiabatic curve in the initial state and the vibrational levels in the well of the final ionic state. Region II: a diabatic curve for A_2^* penetrates into the continuum and undergoes autoionization.

investigated in a merging beam experiment by Ringer and Gentry.[14] In the thermal range the relative kinetic energy E_k of the reactants is not sufficient for the total energy to reach the ionic asymptotic limit ($A^+ + A$) and the nuclei remain bound, forming an associative ion $A_2{}^+$. The origin of the ionization must be sought in the couplings between the relevant potential-energy curves for the excited neutral molecule A_2^* and the ground state of the molecular ion $A_2{}^+$.

An essential aspect is the determination of the nature of the interaction between a neutral state A_2^* and the ionic one, as well as the region in which this interaction is important. Nielsen and Berry,[15] and later Koike and Nakamura,[16] in their work on H_2^* considered the vibronic coupling between attractive neutral curves and the $X\,^1\Sigma_g^+$ state of $H_2{}^+$, in a region in which they are close together (denoted by I in Fig. 1). Their calculations were performed in a basis of adiabatic states, neglecting the dynamical couplings with upper states. The cross sections calculated in this way exhibit a monotonically decreasing behavior with increasing kinetic energy E_k and values of about 10^{-18} cm^2 at 300 K. Cohen developed a different interpretation,[17] inspired by the qualitative discussion of Mulliken.[18] He considered repulsive diabatic states He_2^* penetrating into the continuum of $He_2{}^+(X_u^{2+}) + e^-$ and interacting with the attractive ones by electronic coupling. The ionization was hypothesized to occur with a high probability each time the continuum was reached (in a region such as II in Fig. 1), and the transitions between bound states of He_2^* were calculated in the Landau-Zener formulation. The cross sections for HMI and excitation transfer were then calculated as a function of E_k for the $He^*(3,4\,^3L) + He$ systems ($L = 0,1,2$). They exhibit extensive structures related to the crossings between different potential curves, and their thermally averaged values, of the order of magnitude of 10^{-16} cm^2, agree well with the experimental results for $n = 3$.[9,11,12(a)] (In the case when $n = 4$, the only available experimental results[12(b)] should be considered as maximum values rather than absolute ones.) For N^*O, a theoretical interpretation has been developed by Nielsen and Dahler,[19] which is very similar to that of Cohen for He_2^*.

II. EXPERIMENT

Although it seems, from the preceding discussion, that the interpretation given by Cohen explains the experimental data, the structures in the energy dependence of the calculated cross sections $\sigma(E_k)$ have never been observed experimentally. In the averaging procedure such structures are completely obscured. For this reason we have undertake an experimental study of the energy dependence of $\sigma(E_k)$ in a time-of-flight crossed-beam experiment for the collision $He(5\,^3P) + He$.

A. Experimental setup

A preliminary investigation has been reported in a previous paper,[20(a)] in which the velocity distribution of the excited atoms $He(5\,^3P)$ in the reaction chamber was calculated from that of the metastable atoms. This calculation was based on the geometrical parameters of the metastable (initial-state) atom beam and on the characteristics (intensity, divergence, spot size) of the photoexciting laser. However, the different hypothesis used had a particularly important effect at higher energies, so that the experimental cross section was not completely reliable in this range. In the second investigation we therefore introduced photoionization techniques which allowed us to do the following:

(i) optimize the electrostatic lenses for the extraction of the ions, in order to obtain an efficiency independent of the initial energy of these ions (see Sec. II B 1), and

(ii) detect the excited states $He(5\,^3P)$, in order to obtain direct information on their velocity distribution (see Sec. II B 2).

The experimental setup is presented in Fig. 2. As before,[20] we use the three-crossed-beams configuration. The metastable atom beam intersects at right angles the effusive target beam. The common axis of the two lasers used is perpendicular to the atomic beams.

The first laser of the cw, uv type, tunable around 294 nm (photon energy: 4.21 eV). The excited $5\,^3P$ states are produced by photoexcitation from the $2\,^3S$ state. Furthermore, this laser can photoionize the singlet metastable states $2\,^1S$ (ionization potential: 3.97 eV), a procedure which is used to optimize the electrostatic optics. The uv radiation (3—5 mW) was produced by second harmonic generation in a ring laser.[21]

The second laser is an ionized krypton laser, tuned to the red lines (647 and 752 nm). It is used to photoionize the excited $5\,^3P$ states, thus providing a detection method. We checked that under our experimental conditions, fluorescence detection could not provide sufficient signal. The spot size of the red laser is increased so that its intensity variations are less than ~10% over the full width at half maximum of the spatial profile or the uv beam.

The relevant excited states of helium and the different laser wavelengths are illustrated in Fig. 3.

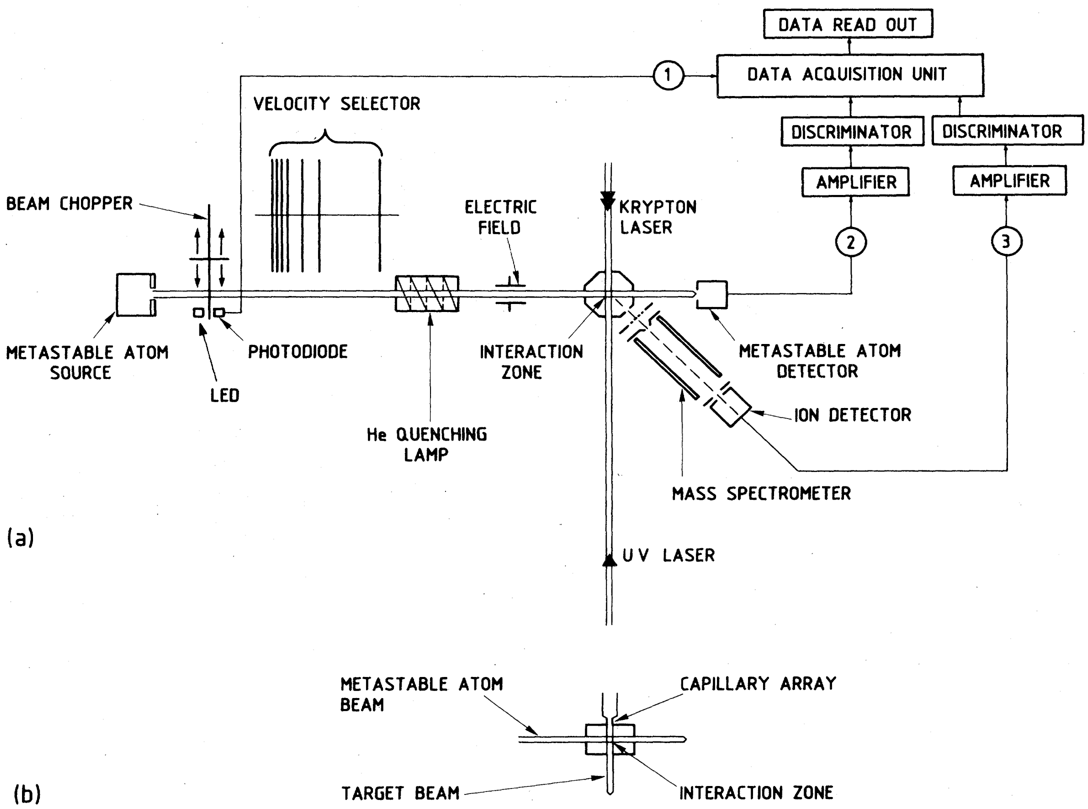

FIG. 2. Schematic representation of the time-of-flight, crossed-beam apparatus. (a) Horizontal plane, (b) vertical plane. The data acquisition unit is coupled to a microcomputer, which also drives the uv laser frequency (see Ref. 20).

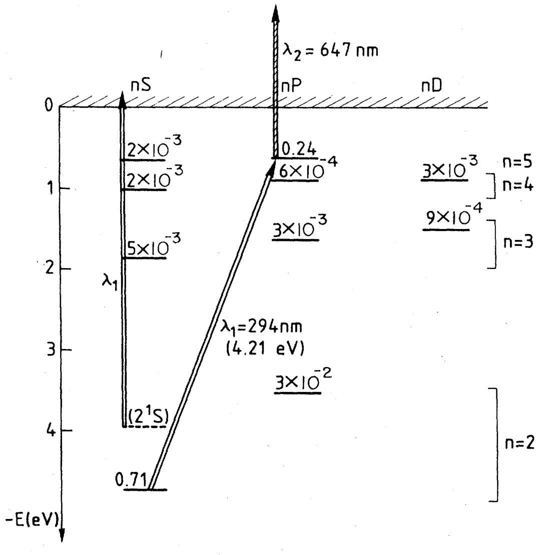

FIG. 3. Partial term diagram showing the relevant levels for the experiment and the role of the two laser wavelengths. The numbers above the levels give typical populations (for atoms with a velocity of 2500 $\mathrm{m\,s^{-1}}$).

B. Time-of-flight procedure

Velocity dependence is investigated using the well-known time-of-flight (TOF) method;[22] the presence of excited states and the introduction of photoionization measurements are, however, worth considering in detail.

The rotation of the chopper slits in front of the fixed slits on the metastable beam generates a gate function $A(t)$ during which a burst of atoms is transmitted. For a nominal time of flight (τ), a metastable atom flux Φ^m is created in the collision chamber:

$$\Phi^m(\tau) \propto \int_{-\infty}^{+\infty} A(t)\dot{\phi}_v^m(v)dv \ , \tag{3}$$

where $\dot{\phi}_v^m$ is the velocity distribution of the metastable atom flux emerging from the source, $v = L/(\tau - t)$ the velocity of atoms having crossed the chopper at time t, and L is the distance between the chopper and the chamber. The gate function with a half-maximum width of 5 μs appears to be equivalent to a Dirac peak and Eq. (3) reduces to

$$\Phi^m(\tau) \propto \dot{\phi}_v^m(L/\tau)\frac{L}{\tau^2} \ , \tag{4}$$

where τ is related to the velocity by $v = L/\tau$.

1. *TOF with He(2^1S): Test of extraction optics*

With an electron multiplier positioned along the metastable beam axis (Fig. 2), it is possible to detect the flux $\Phi^m(\tau')$ at a distance L' from the chopper, with

$$v = L/\tau = L'/\tau' \tag{5a}$$

and

$$L/\tau^2 = v^2/L \ , \tag{5b}$$

and therefore possible to derive the flux $\Phi^m(\tau)$

$$\Phi^m(L/v) \propto \Phi^m(L'/v')\frac{L'}{L} \ . \tag{6}$$

On the other hand, as we already seen, uv laser photons can ionize the 2^1S states, as follows:

$$\mathrm{He}(2^1S) + (h\nu)_{\mathrm{uv}} \rightarrow \mathrm{He}^+ + e^- \ . \tag{7}$$

By detecting the photoions from this reaction we obtain a TOF signal given by

$$N^+(\tau) \propto \dot{n}_v^m(L/\tau)\frac{L}{\tau^2} \ , \tag{8}$$

where $\dot{n}_v^m$ is the velocity distribution of the metastable (2^1S) density in the beam, as the photoionization measurement is sensitive to the atomic density. From the simple relation

$$\dot{n}_v^m = \dot{\phi}_v^m / v \tag{9}$$

we derive

$$N^+(\tau) \propto \Phi^m(\tau)\tau \ . \tag{10}$$

This relation holds under two conditions.

(i) The metastable atom flux velocity distribution is the same for singlet and triplet species (this has been verified many times in our experiments).

(ii) The extraction of ions from the chamber and the transit through the mass spectrometer do not depend on the initial energy of the ions in the chamber.

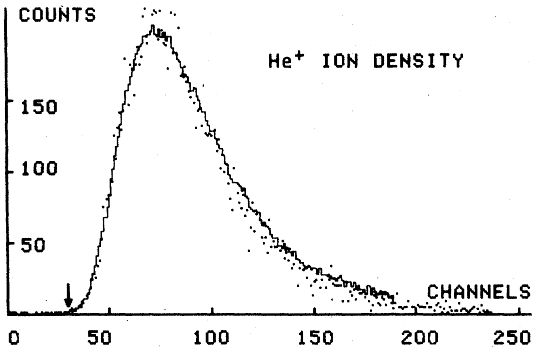

FIG. 4. TOF spectra illustrating how the ion optics are tested. Points represent the He$^+$ photoion counting [Eq. (7)]. The solid curve is derived from the metastable atom flux [right-hand term in Eq. (10)] and normalized on the points. The abscissa is the time of flight measured on a scale of 256 channels 2-μs wide. The test is especially critical in the high-energy part (arrow).

A comparison of experimental TOF spectra with metastable atom and photoion detection is presented in Fig. 4. The two curves superpose perfectly, illustrating Eq. (10). This provides a powerful test of the optimization of the electrostatic lenses.

2. *TOF with He(5^3P): Derivation of the cross section*

We now consider TOF measurements with excited He(5^3P) atoms. In the interaction chamber the uv photoexcitation of the metastable He(2^3S) atoms

$$\mathrm{He}(2^3S) + (h\nu)_{\mathrm{uv}} \rightarrow \mathrm{He}(5^3P) \tag{11}$$

creates a flux of excited states Φ^* depending on Φ^m and on the uv laser parameters. These excited atoms react with target atoms in accordance with Eq. (1), and the $\mathrm{He_2}^+$ ions ($m = 8$ amu) produced give a TOF signal

$$N_8^+(\tau) \propto \sigma_{\mathrm{eff}}(v) \int_\Sigma \Phi^* d\Sigma \ , \tag{12}$$

Σ being the area of the metastable beam illuminated by the uv laser and $\sigma_{\mathrm{eff}}(v)$ the effective cross section (in the laboratory frame).

When the red laser is used to photoionize the excited He(5^3P) atoms

$$\mathrm{He}(5^3P) + (h\nu)_{\mathrm{red}} \rightarrow \mathrm{He}^+ + e^- \tag{13}$$

we obtain a TOF signal from the photoions He$^+$ ($m = 4$ amu) produced:

$$N_4^+(\tau) \propto \int_\Sigma n^* d\Sigma \ , \tag{14}$$

which is directly related to the excited atom density $n^* = \Phi^*/v$. Comparing Eqs. (12) and (14), we derive

$$\sigma_{\mathrm{eff}}(v) \propto N_8^+ / N_4^+ v \tag{15a}$$

or

$$\sigma_{\mathrm{eff}}(L/\tau) \propto \tau N_8^+ / N_4^+ \ . \tag{15b}$$

Thus we can eliminate the velocity and spatial dependences arising in $\int_\Sigma \Phi^* d\Sigma$ and extract the velocity dependence of $\sigma_{\mathrm{eff}}(v)$. The same procedure as in previous papers[20,22] is used to derive $\sigma(v_r)$ from $\sigma_{\mathrm{eff}}(v)$, v_r being the relative velocity of the colliding atoms.

The TOF spectra N_4^+ and N_8^+ are reported in Fig. 5; the cross section σ is plotted as a function of the relative kinetic energy in Fig. 6. In order to reduce the counting rate dispersion, the 256 channels 2-μs wide of the TOF spectra have been grouped into 128 channels 4-μs wide. Only the central section of the TOF spectra with significant counts is conserved. Each point in Fig. 6 represents the content of such a 4-μs-wide channel. Some typical error bars are shown; their height represents the statistical error (± one standard deviation). As usual in crossed-beam experiments, we obtain only relative values for the cross section, and the experimental curve in Fig. 6 has been normalized to the one calculated in Sec. III.

Comparison with the result of our previous experiment (Fig. 3 in Ref. 20) shows that the cross sections are identical in the range $20 \le E_k \le 80$ meV. The decrease in the cross section for $E_k > 80$ meV, observed previously, is not confirmed in the present work. It was due to the following:

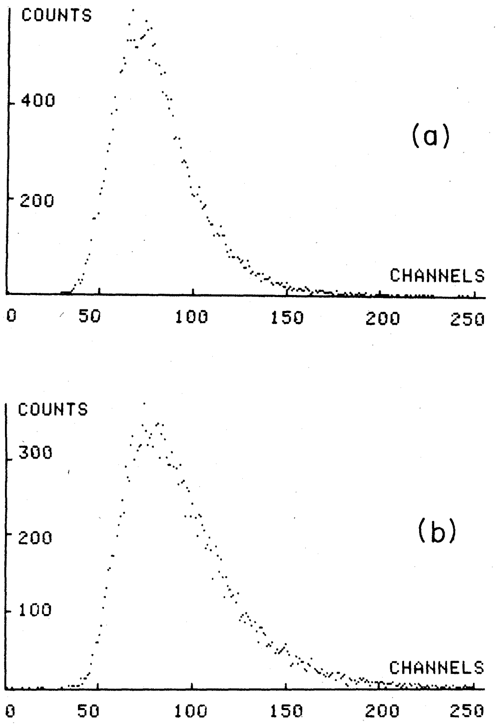

FIG. 5. TOF spectra used to extract the ionization cross section (channel width is 2 μs). (a) Associative ions $He_2{}^+$, accumulation time 1.5 h; (b) He^+ photoions from the reaction in Eq. (13), accumulation time 13.5 h.

(i) Distortion between the metastable and excited state velocity distributions greater than that calculated, and

(ii) poor efficiency of the extraction optics for a high initial ion energy.

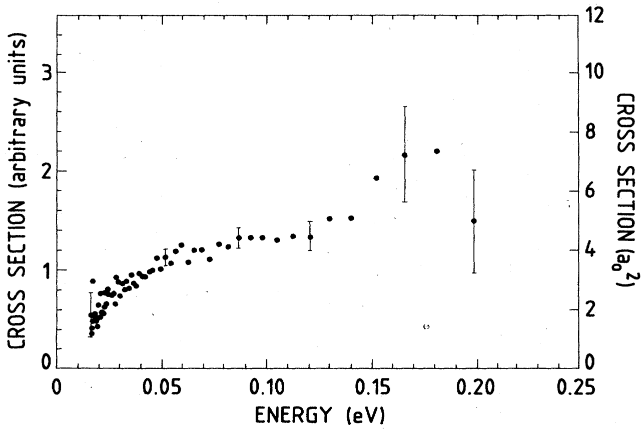

FIG. 6. HMI cross section as a function of the relative kinetic energy E_k. Each point represents the content of a 4-μs-wide channel. Some typical error bars are shown; their height is determined by ± one standard deviation in the counts. Our results are relative; the absolute scale shown on the right-hand side of the figure is obtained by normalizing our experimental cross section to the one calculated in Sec. III.

These two problems have been avoided in this work by the introduction of photoionization techniques. Per contra, this method is sensitive to the excited states density, and not the flux as before, and provides a signal N_4^+ which falls to zero more rapidly with increasing energies (due to the factor $1/v$). For this reason the energy range in Fig. 6 terminates at 0.2 eV instead of 0.35 eV as in Ref. 20. However, the fact that the cross section tends to increase rather than drop to zero is in good qualitative agreement with the predictions of Cohen[17] for the excited states 3^3P and 4^3P.

III. CALCULATIONS

A comparison of our experimental results in Fig. 6 with the cross sections for lower states calculated by Cohen can hardly be said to show more than a qualitative similarity. Since this model is based on (quasi)diabatic states for the He_2^* molecule, we shall first discuss their general structure; we shall then recall the main features of the model and extend it to the system studied here.

A. Diabatic states of He_2^*

Such states can be constructed by the addition of a weakly bound Rydberg electron to the ionic core $He_2{}^+$ found in one of its two first states: (i) the ground state $X^2\Sigma_u^+$, attractive, and (ii) the first excited state $A^2\Sigma_g^+$, repulsive. Such He_2^* states have been discussed by Mulliken,[18] Steets and Lane[23] (who also presented a qualitative discussion of HMI), and Guberman and Goddard in their extensive *ab initio* calculations.[24] For intermediate values of the internuclear separation (of the same order of magnitude as the equilibrium distance for $He_2{}^+$, $R_e \cong 2a_0$), the total wave function is well approximated by

$$|\phi_{nlm}(1s'_A 1s_B \overline{1s_B} \pm 1s'_B 1s_A \overline{1s_A})| \,, \tag{16}$$

where ϕ_{nlm} is the Rydberg electron orbital from the excited atom at the separated atom limit and $1s$ and $1s'$ are orbitals of the ionic core electrons; the vertical bars refer to a Slater determinant, and the ± sign determines the g or u parity. A and B are the centers of the nuclei; ϕ_{nlm} is centered about the midpoint of AB.

The shape of the potential curves is essentially determined by that of the ionic core and can be derived from elementary symmetry considerations (see Table I). A molecular diabatic state for which the parity relative to the inversion operator (denoted by indices u or g) and that of the Rydberg angular momentum $(-1)^l$ are the same (opposite) is repulsive (attractive).

The diabatic energies can be rather accurately described

TABLE I. Determination of the attractive (A) or repulsive (R) character of the quasidiabatic states of He_2^*.

Core $He_2{}^+$	$^2\Sigma_u^+$		$^2\Sigma_g^+$	
$(-1)^l$	+	−	+	−
Parity of He_2^*	u	g	g	u
Character	A	A	R	R

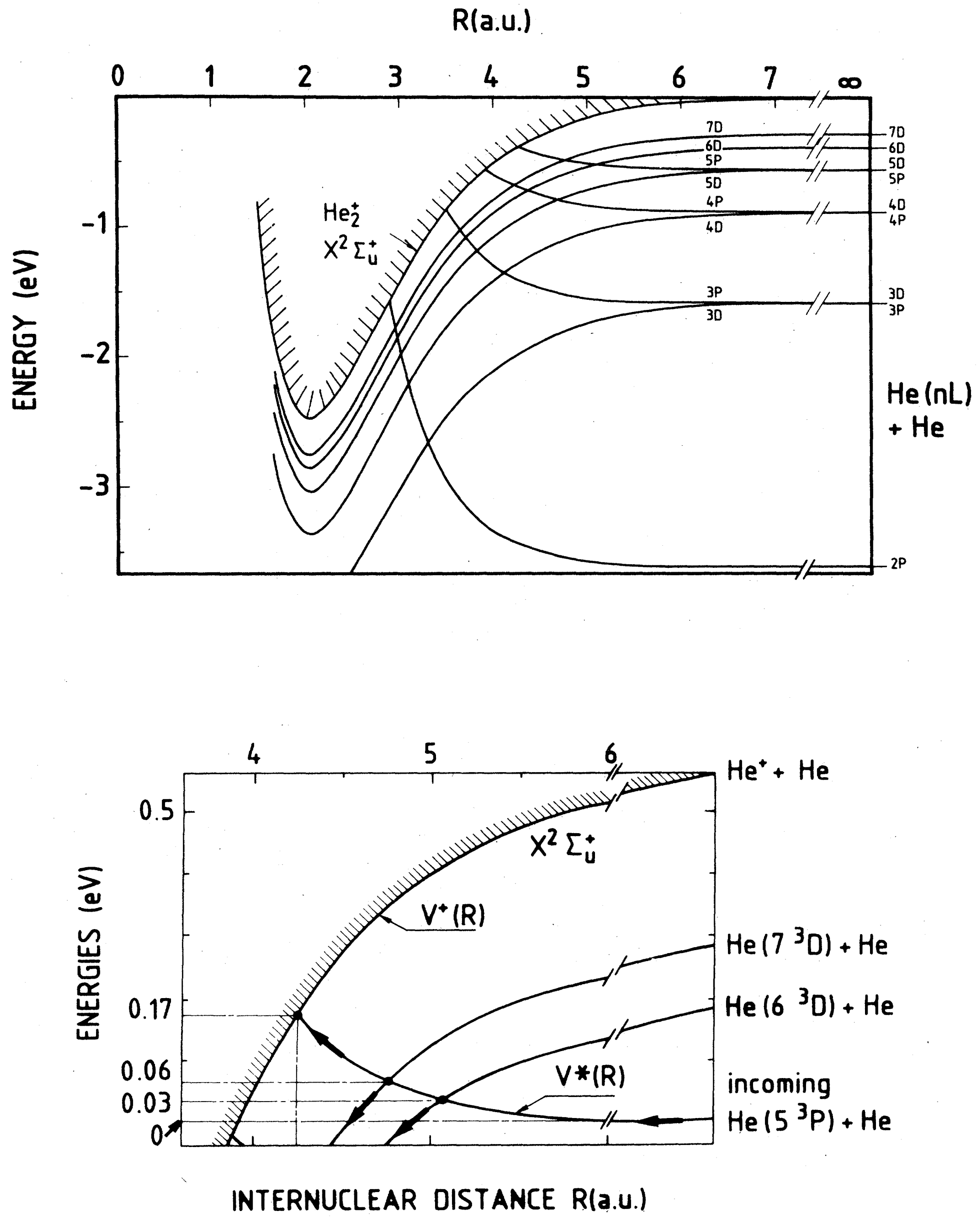

FIG. 7. Diabatic potential energies for He$_2^*$ obtained by shifting the ionic energy curves. The ground state He$_2{}^+(X^2\Sigma_u^+)$ is also represented. In this approximation the Σ and Π states are degenerate. Only states resulting from He($n\,^3P,D$)+He are represented for clarity, since they give the most important contribution to the cross section. The lower part is an enlargement of the region around the incoming channel He($5\,^3P$)+He.

for intermediate R values by adding the binding energy in the separated-atom limit to the He$_2{}^+$ core energies. Some of such potential curves for our system are presented in Fig. 7.

B. The multistate curve-crossing model

A multistate curve-crossing (MSCC) model has been developed by Cohen[17] in the framework of the diabatic states of He$_2^*$. It is based on the following hypothesis.

(i) Nuclear motion is treated classically.

(ii) Bound-bound transitions in the diabatic states are considered to be localized at the crossings and treated by the Landau-Zener formulation. The angular coupling contribution is negligible.

(iii) Bound-free electronic transitions (ionization) occur with a probability equal to 1 each time the continuum is reached (this assumption is not essential).

With these assumptions, a probability $P(b)$ is calculated for each impact parameter b and the cross section for a given molecular symmetry $^3\Lambda_{u,g}$ $n\,^3L$ derived in the usual way:

TABLE II. Molecular symmetries giving repulsive potential curves for different separated-atom limits.

Separated-atom limit	Symmetries
He($n\,^3S$)+He	$^3\Sigma_g$
He($n\,^3P$)+He	$^3\Sigma_u$, $^3\Pi_u$
He($n\,^3D$)+He	$^3\Sigma_g$, $^3\Pi_g$, $^3\Delta_g$

$$Q(^3\Lambda_{u,g}\; n\,^3L)=2\pi\int_0^\infty P(b)b\,db\;. \tag{17}$$

For a given collision He($n\,^3L$)+He, the cross section is the sum of the contributions of all possible molecular symmetries:

$$\sigma(n\,^3L)=\frac{1}{2L+1}\sum_{\Lambda=0}^{L}\tfrac{1}{2}g_\Lambda[Q(^3\Lambda_g\; n\,^3L)+Q(^3\Lambda_u\; n\,^3L)]\;, \tag{18}$$

where $g_0=1$, $g_{\Lambda\neq 0}=2$, and $\frac{1}{2}g_\Lambda(1/2L+1)$ is a statistical weight for a symmetry $^3\Lambda_{u,g}\; n\,^3L$.

The cross sections calculated in this way exhibit some characteristic structures.

(i) Each time the relative kinetic energy E_k becomes sufficient to overcome a crossing between a repulsive incoming channel and the ionization limit $He_2{}^+(X\,^2\Sigma^+)$, the cross section may increase strongly, because the continuum is directly accessible. These crossing energies will be referred to as diabatic thresholds.

(ii) In the vicinity of diabatic thresholds the shape of the cross section is determined mainly by the contribution of molecular symmetries in which the incoming channel is repulsive. These symmetries are listed in Table II.

(iii) The diabatic thresholds of different Σ states are close together, because these states are almost degenerate. However, for systems with nonzero angular momentum L, the Σ-states contribution is not determinant for the shape of the cross section near the diabatic thresholds. This is due to the strongly adiabatic character of the crossings between repulsive and attractive Σ states.

C. Extension to He($5\,^3P$)+He

In the following, the diabatic states correlated to the separated-atom limit He($n\,^3L$)+He will be denoted by $n\,^3L$.

From the potential curves represented in Fig. 7, we obtain a value of $E_k=0.17$ eV for the diabatic threshold (in this representation the $^3\Sigma$ and $^3\Pi$ states are degenerate). This value can be compared with $E_k=0.16$ eV where we observe an increase in the measured cross section. Moreover, our experimental points fall in an energy range close to the diabatic threshold. Following the discussion in Sec. III B, we would expect the shape of the calculated cross section to be mainly determined by the contribution of the $^3\Pi_u$ channels.

A model potential method for the He_2^* molecule has been developed in our laboratory and tested by calculating the $b\,^3\Pi_g$ and $f\,^3\Pi_u$ adiabatic potentials.[25] This method has been applied to the calculation of $^3\Pi_u$ diabatic states and couplings between them;[26] they are listed in Table III.

TABLE III. Curve-crossing parameters for $^3\Pi_u$ symmetry. All quantities are in atomic units.

States	R_x	$E(R_x)^a$	$V_{12}(R_x)$	$\Delta\left[\frac{dV}{dR}\right]_{R_x}$
2P-3D	3.14	−0.0916	-1.91×10^{-2}	0.1029
-4D	2.97	−0.0791	-9.87×10^{-3}	0.1317
-5D	2.85	−0.0754	$+6.76\times10^{-3}$	0.1580
-5G	2.84	−0.0746	$+3.28\times10^{-4}$	0.1578
-6D	2.82	−0.0719	$+4.93\times10^{-3}$	0.1594
-6G	2.81	−0.0714	$+3.16\times10^{-4}$	0.1588
-7D	2.80	−0.0699	$+3.82\times10^{-3}$	0.1696
-7G	2.80	−0.0695	$+2.79\times10^{-4}$	0.1692
-8D	2.79	−0.0685	$+3.08\times10^{-3}$	0.1698
-8G	2.79	−0.0682	$+2.42\times10^{-4}$	0.1696
-ion	2.75	−0.0642		
3P-3D	5.64	−0.0568	-1.91×10^{-4}	0.0035
-4D	4.04	−0.0450	$+4.23\times10^{-3}$	0.0372
-5D	3.72	−0.0440	$+2.77\times10^{-3}$	0.0620
-5G	3.71	−0.0435	-7.38×10^{-5}	0.0613
-6D	3.62	−0.0410	$+2.08\times10^{-3}$	0.0620
-6G	3.62	−0.0408	-8.47×10^{-6}	0.0616
-7D	3.57	−0.0392	$+1.64\times10^{-3}$	0.0668
-7G	3.57	−0.0391	$+1.86\times10^{-5}$	0.0666
-8D	3.54	−0.0381	$+1.33\times10^{-3}$	0.0716
-8G	3.54	−0.0379	$+2.83\times10^{-5}$	0.0716
-ion	3.46	−0.0342		

TABLE III. (*Continued*).

States	R_x	$E(R_x)$[a]	$V_{12}(R_x)$	$\Delta\left(\dfrac{dV}{dR}\right)_{R_x}$
$4F$-$5D$	4.53	-0.0295	$+3.51\times10^{-4}$	0.0147
-$5G$	4.50	-0.0294	$+2.76\times10^{-3}$	0.0144
-$6D$	4.25	-0.0275	$+2.61\times10^{-4}$	0.0256
-$6G$	4.24	-0.0273	$+1.59\times10^{-3}$	0.0254
-$7D$	4.13	-0.0261	$+1.99\times10^{-4}$	0.0310
-$7G$	4.12	-0.0260	$+1.09\times10^{-3}$	0.0310
-$8D$	4.06	-0.0251	$+1.58\times10^{-4}$	0.0336
-$8G$	4.06	-0.0250	$+8.20\times10^{-4}$	0.0334
-ion	3.89	-0.0218		
$4P$-$4D$	6.34	-0.0319	-3.88×10^{-5}	0.0016
-$5D$	4.54	-0.0295	$+1.31\times10^{-3}$	0.0156
-$5G$	4.51	-0.0293	-4.18×10^{-5}	0.0154
-$6D$	4.27	-0.0272	$+1.09\times10^{-3}$	0.0268
-$6G$	4.26	-0.0271	-5.54×10^{-4}	0.0266
-$7D$	4.15	-0.0257	$+8.82\times10^{-4}$	0.0323
-$7G$	4.14	-0.0256	-3.74×10^{-5}	0.0323
-$8D$	4.08	-0.0247	$+7.29\times10^{-4}$	0.0350
-$8G$	4.08	-0.0246	-2.42×10^{-5}	0.0348
-ion	3.91	-0.0213		
$5P$-$5D$	6.98	-0.0206	-7.60×10^{-6}[b]	0.0005[b]
-$5G$	6.77	-0.0206	-3.70×10^{-6}[b]	0.0005[b]
-$6D$	5.00	-0.0195	$+5.77\times10^{-4}$	0.0094
-$6G$	5.00	-0.0194	-2.40×10^{-5}	0.0094
-$7D$	4.69	-0.0184	$+5.22\times10^{-4}$	0.0152
-$7G$	4.68	-0.0183	-3.27×10^{-5}	0.0152
-$8D$	4.55	-0.0176	$+4.47\times10^{-4}$	0.0182
-$8G$	4.55	-0.0175	-2.76×10^{-5}	0.0182
-ion	4.24	-0.0147		
$5F$-$5G$	7.00	-0.0206	0[b]	0[b]
-$6D$	5.00	-0.0194	$+2.15\times10^{-4}$	0.0090
-$6G$	4.98	-0.0194	$+1.06\times10^{-3}$	0.0090
-$7D$	4.69	-0.0184	$+1.78\times10^{-4}$	0.0144
-$7G$	4.67	-0.0184	$+7.89\times10^{-4}$	0.0144
-$8D$	4.55	-0.0177	$+1.45\times10^{-4}$	0.0176
-$8G$	4.54	-0.0176	$+6.17\times10^{-4}$	0.0176
-ion	4.22	-0.0149		

[a] Relative to He-He$^+$ separated-atom energy.

[b] Used in the MSCC model (dashed line in Fig. 9). The values taken in the modified MSCC model including long-range couplings [(b) in Sec. IV and solid line in Fig. 9(b)] are $V_{12}(R_x)=2.0\times10^{-3}$ and $\Delta(dV/dR)_{R_x}=10.0$ for the three $5P$-$5D$, $5P$-$5G$, and $5F$-$5G$ crossings.

The diabatic energies are very close to those obtained in Sec. III A; the greatest difference in crossing energies is found for the diabatic threshold, which changes from 0.17 to 0.16 eV. The couplings, thus obtained in a somewhat easier way than by the *ab initio* calculation of Cohen,[17] are in good agreement with the results of the latter for the lower states.[26]

For the treatment of collision dynamics, we used the MSCC model.[17] We note that the couplings between $n\,^3P$ and $n'\,^3D$ states are between one and two orders of magnitude greater than any other coupling; this has a drastic effect on the Landau-Zener probability at the crossing between states i and j:

$$P_{ij}=e^{-2\pi\gamma} \tag{19a}$$

with

$$\gamma=\frac{|V_{ij}|^2}{v_r\,\Delta F}\,, \tag{19b}$$

where V_{ij} is the coupling, v_r the relative velocity, and ΔF the difference between the potential curve slopes at the crossing point.

The role of the closed attractive channels is of particular importance as illustrated in Fig. 8; such channels generate a strong effective coupling between the entrance channel and the lower states and give rise to the nonvanishing cross section below the diabatic threshold. The efficiency of this effective coupling falls to zero when the attractive channel opens.

In addition to using the analytic formulation of Ref. 17, we have numerically calculated the evolution of the partial fluxes on the $n\,^3P$ and $n'\,^3D$ channels (F and G states were retained only in analytic calculations). This somewhat more intuitive approach, described in the Appendix, corroborates the analytic evaluations. The numerical approach is probably more amenable to Monte Carlo simulation, although this was not done in the present work.

The solution for the different impact parameters gives the probability $P(b)$. After integration as in Eq. (17), we derive the contribution of the $^3\Pi_u$ channels to the cross section, including the weighting factor as in Eq. (18):

$$\tfrac{1}{3}Q(^3\Pi_u\,5^3P)\ . \tag{20}$$

The result (dashed line) is shown in Fig. 9. The experimental results obtained in Sec. II (shown by points in Fig. 6) are represented in Fig. 9 by rectangles for a more precise comparison with theoretical results. The height of the rectangles equals the height of the error bars in Fig. 6 and represents the statistical error (± one standard deviation), while the width represents the uncertainty in energy resulting from the channel width, which was set to 4 μs. The other contributions to the errors are negligible. The experimental results are normalized to the calculated cross section at $E_k = 0.12$ eV. We observe fairly good agree-

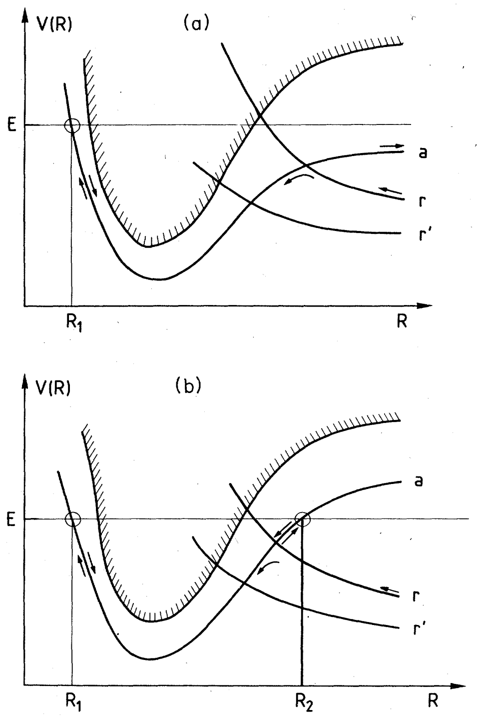

FIG. 8. Evolution of the flux on an attractive channel a. r is the repulsive incoming channel, and r' is a lower repulsive channel. (a) a is open. Part of the incoming flux on r goes on a at the crossing and is then reflected at the turning point R_1. This flux is then lost by dissociation on $a,r,r',\ldots$. Only a very small fraction reaches the continuum via r'. (b) a is closed. Part of the incoming flux on r goes on a at the crossing and is then trapped between the two turning points R_1,R_2, and crossings such as a-r' are encountered a great number of times. Thus, the closed channel a couples very efficiently the incoming channel r with the continuum via r', even if the diabatic threshold on r is inaccessible.

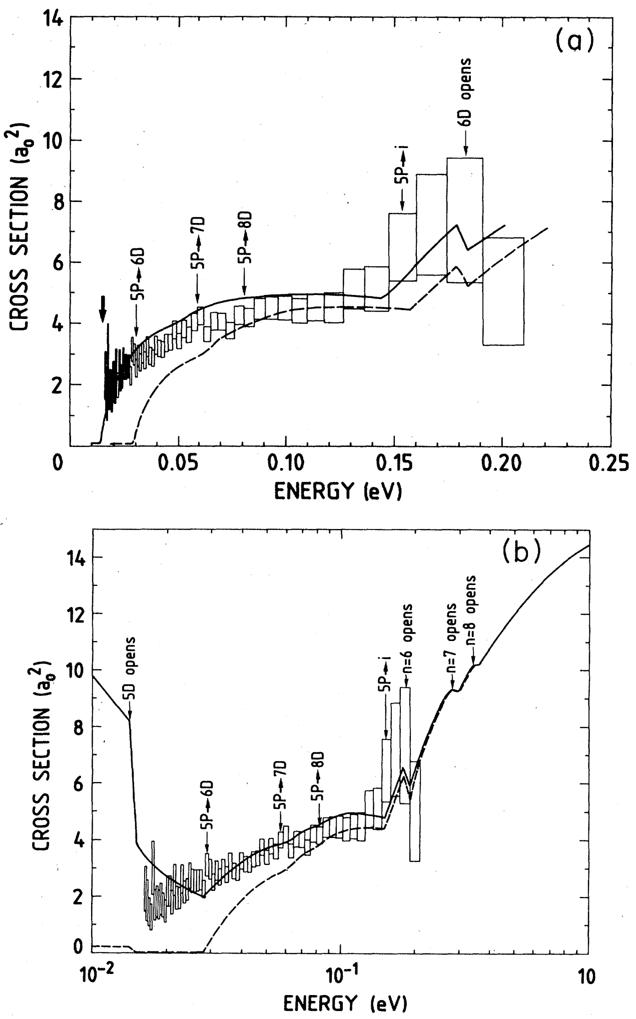

FIG. 9. (a) Calculated HMI cross sections as a function of the relative kinetic energy. Dashed line results from MSCC method and solid line results from MSCC method including a 14-meV shift of the crossing energies [see (a) in Sec. IV]. Important features are designated by arrows. The thick arrow shows the approximate location of the $^3\Sigma_u$ ($5P$-$6S$) crossing. The experimental results are shown by rectangles in order to take into account the uncertainty in energy resulting from the channel width (4 μs). (b) Calculated HMI cross section extended to lower and higher (relative) kinetic energies. Dashed line results from MSCC method and solid line results from modified MSCC method including long-range couplings [see (b) in Sec. IV]. Experimental points: as in (a).

ment between the experimental and theoretical results, which confirms the validity of the model. Improvement of the calculation at the lowest energies is discussed in Sec. IV. As expected, the energy dependence of the cross section in this range is mostly determined by the contribution of the $^3\Pi_u$ channels.

IV. RESULTS AND DISCUSSION

As there is good agreement between the measured and calculated curves in Fig. 9, a detailed study of the calculated cross section can be used to determine the mechanisms responsible for HMI in different part of the kinetic-energy range.

(*1*) *First threshold at 30 meV.* The first crossing with an attractive curve ($6D$), which is a closed channel, is reached (see Fig. 7). Note that the $5P$-$5D$ crossing is situated below the asymptotic limit of the $5P$ state.

(*2*) *Threshold around 60 meV.* This threshold corresponds to the second crossing ($5P$-$7D$) (see Fig. 7). The next one ($5P$-$8D$) has little effect on the calculated curve. This demonstrates the convergence of the calculation with respect to the inclusion of attractive channels.

(*3*) *Threshold at 0.16 eV.* This is the diabatic threshold—crossing of the $5P$ with the continuum limit—obtained from the potential curves calculated using the model potential method.

(*4*) *Dip at 0.185 eV.* The cross section increases after the diabatic threshold and then decreases slightly after the opening of the exit channel $6D$ at 0.181 eV. The flux which was previously trapped, when this channel was closed, is now lost through a dissociation process leading to $\mathrm{He}(6^3D)+\mathrm{He}$ (see Sec. III C and Fig. 8). The cross section then goes on increasing, due to direct penetration into the continuum via the entrance channel.

One can define an intermediate zone between the diabatic threshold at 0.16 eV and the opening of the channel $6D$ at 0.18 eV. Below this zone HMI is mainly due to a path $5P$-$6D$-nP ionization (with $n=2,3$, or 4), with adiabatic transitions at diabatic bound state crossings. Above the intermediate zone, the mechanism is mostly diabatic ($5P\rightarrow$ionization). The shape of the cross section between 0.16 and 0.18 eV, resulting from a competition between the two mechanisms, is obviously not an interference pattern since the nuclear motion is treated in a purely classical way.

A slight mismatch between the experimental and calculated MSCC (dashed line) cross sections is evident near the apparent threshold in Fig. 9; several origins can be responsible for it.

(a) We consider the effect of an inaccuracy in the energies calculated by the model potential method. To investigate the importance of this effect, we calculated the cross section after a uniform shift of all the crossing energies of the incoming $5P$ channel. (This is justified by the fact that the potential curves are nearly linear in the considered region.) In Fig. 9(a) the result (solid line) for a shift of 14 meV towards lower energies is given. Experimental thresholds are thus well reproduced.

(b) The interaction has been discussed in a framework in which all transitions are strictly localized and Eq. (19b) is applicable. This is probably adequate except for long-range crossings between asymptotically nearly degenerate potential curves. In particular, collisional mixing of the different states arising from the $n=5$ limit is expected to be important in the $\mathrm{He}(5^3P)+\mathrm{He}$ reaction. Clear evidence for long-range couplings between these states has been provided by the observation of large inelastic cross sections (larger than πR_x^2 where R_x is the crossing distance) for transitions between them.[27] The simple curve-crossing calculation gives inelastic cross sections, for transitions between states having the same principal quantum number, which are much too small. The actual transitions occur at distances greater than R_x as well as at R_x. However, if R_x is the largest relevant crossing distance, these two mechanisms may be approximately treated together since they have rather similar velocity dependences [both have terms depending on $\exp(-\mathrm{const}/v)$].[28] We have introduced a single empirical parameter to represent the *effective* coupling [γ in Eq. (19a)] between states dissociating to the $n=5$ limit. With the condition that the ratio of the cross sections at 0.02 and 0.1 eV agree with experiment, we obtain $\gamma_{\mathrm{eff}}=4\times10^{-6}$. The result of this modified MSCC treatment is the solid curve in Fig. 9(b), which is in much improved agreement with experiment at low energies and essentially unchanged at higher energies.

In Fig. 9(b) we show also the results of extending the calculation to energies outside the measured range. Most interesting is the prediction by the modified MSCC calculation of an increase in the HMI cross section at subthermal energies. This increase is due to the increasingly adiabatic behavior at the avoided crossing between the $5P$ and $5D$ potential curves as the collision energy decreases. Adiabatic behavior at this initial avoided crossing then allows access to the ionization continuum via the lower-lying repulsive diabatic curves.

(c) A source of some uncertainty in the present calculations is the participation of other molecular symmetries, in particular the Σ states. Although they are expected to be of lesser importance,[17] their contribution may not be completely negligible. From the approximate potential curves in Fig. 7, one can expect the first crossing $^3\Sigma_u^+(5P\text{-}6S)$ to be around 15 meV.

These effects could be clarified by an extremely accurate calculation of the potential curves (within 1 meV) and their couplings. At this stage the accuracy of the model potential calculations depends on that of the ionic $X^2\Sigma_u^+$ and $A^2\Sigma_g^+$ energies, the contribution of which is approximately additive in the crossing region. The values used for $X^2\Sigma_u^+$ (Ref. 25) result from an *ab initio* calculated curve, shifted downward by 15 meV in the well region to reproduce translational spectroscopy measurements.[29] The calculation of the $^3\Sigma$ states of He_2^* using model or pseudopotential methods[30] is somewhat more tedious than for Π states owing to s electrons in the core, but is in principle possible.

V. CONCLUSION

The mechanisms responsible for Hornbeck-Molnar ionization in the collision

$$\mathrm{He}(5^3P)+\mathrm{He}\rightarrow\mathrm{He}_2{}^+ + e^-$$

have been identified by a direct comparison between experimental and theoretical investigations. In the experimental part we obtained the first evidence of structures arising in the kinetic-energy dependence of the cross-section. This was done using a crossed-beam time-of-flight apparatus, associated with a high-resolution uv laser and a highly sensitive photoionization detection of excited states. It has been possible to calculate the main contribution to the cross section ($^3\Pi_u$ channels) with the use of model potential results for the relevant molecular potentials. The good agreement between experimental and theoretical results confirms the validity of the MSCC model, in which ionization is mainly due to dynamical couplings between bound states of the neutral molecule He_2^*.

In particular, it has been possible to demonstrate the existence of a nonvanishing cross section below the diabatic threshold, essentially due to adiabatic transitions between the bound molecular states and to the important role of closed channels. Just above the diabatic threshold, the opening of the main closed channel ($^3\Pi_u$ 6^3D) makes the adiabatic process inefficient, and it is replaced by a diabatic process: direct penetration into the continuum via the repulsive entrance channel. The calculations including long-range coupling in the initial channel [Fig. 9(b)] predict an increase in the cross section at collision energies (subthermal) lower than obtainable in the present experiment. Verification of this behavior would provide a further test of the model.

ACKNOWLEDGMENTS

We are strongly indebted to J. Morellec and P. de Pujo for lending us the krypton laser.

APPENDIX

Following the discussion in Sec. III, we have also calculated the probability $P(b)$ by a numerical treatment of the multistate curve-crossing problem. In this corroborating calculation we consider only the repulsive ^3P and attractive ^3D channels of symmetry $^3\Pi_u$. Initially, there is a flux equal to unity on the channel 5^3P. We then calculate all the partial fluxes, which are denoted as indicated in Fig. 10.

We verify in the final result (see Fig. 6 and Sec. IV) that the calculation has converged with respect to the inclusion of higher attractive channels. The repulsive states with $n>5$ are situated too high to contribute efficiently to the cross section in our energy range. The attractive states lower than the $5D$ play a role only in the excitation transfers and do not influence the ionization cross section. The partial flux evolution is described by an iterative process, each iteration including four steps.

(*1*) *Decreasing R.* For each *i*-*j* crossing we have localized transitions:

$$X_{i+1,j}=P_{ij}X_{ij}+(1-P_{ij})Y_{ij}\ , \tag{21a}$$

$$Y_{i,j+1}=P_{ij}Y_{ij}+(1-P_{ij})X_{ij} \tag{21b}$$

$$\text{for } i=1,2,\ldots,m \text{ and } j=1,2,\ldots,n\ ,$$

P_{ij} being the Landau-Zener probability [Eq. (19)].

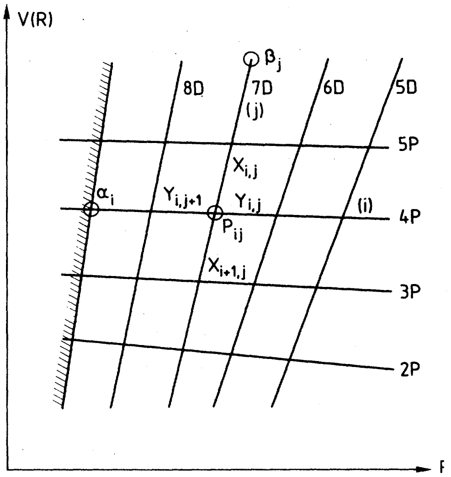

FIG. 10. Schematic representation of the channels involved in the calculation of the cross section. X_{ij}, Y_{ij} are partial fluxes on attractive and repulsive curves; P_{ij} is the Landau-Zener probability [Eq. (19)]. α_i,β_j are the ionization and dissociation probabilities as defined in the text.

(*2*) *Ionization or reflection at small R.* At the *k*th iteration, part of the total flux is ionized:

$$I_k=\sum_{i=1}^{m} Y_{i,m+1}\alpha_i\ , \tag{22}$$

where α_i is 1 or 0 depending on whether the crossing of the *i*th channel with $X^2\Sigma_u^+$ is accessible or not. The partial fluxes are reflected at the inner turning points, or lost, which is described by

$$X_{n+1,j}\leftarrow X_{n+1,j}\ ,\quad j=1,2,\ldots,n \tag{23a}$$

$$Y_{i,m+1}\leftarrow(1-\alpha_i)Y_{i,m+1}\ ,\quad i=1,2,\ldots,m\ . \tag{23b}$$

(*3*) *Increasing R.* As in (1) localized transitions exist:

$$X_{ij}=P_{ij}X_{i+1,j}+(1-P_{ij})Y_{i,j+1}\ , \tag{24a}$$

$$Y_{ij}=P_{ij}Y_{i,j+1}+(1-P_{ij})X_{i+1,j} \tag{24b}$$

$$\text{for } i=m,m-1,\ldots,1 \text{ and } j=n,n-1,\ldots,1\ .$$

(*4*) *Dissociation or reflection on closed channels.* Part of the flux is lost by dissociation on all the open channels:

$$L_k=\sum_{i=1}^{m} Y_{i,1}+\sum_{j=1}^{n} X_{i,j}\beta_j\ , \tag{25}$$

where β_j equals 0 on closed attractive channels and β_j equals 1 on open ones. The partial fluxes are reflected at the outer turning points, or lost:

$$X_{1,j}\leftarrow(1-\beta_j)X_{1,j}\ ,\quad j=1,2,\ldots,n \tag{26a}$$

$$Y_{i,1} \leftarrow 0\ , \quad i=1,2,\ldots,m\ . \tag{26b}$$

When a crossing i-j becomes inaccessible due to centrifugal barriers, turning points appear in the i and j channels under the crossing. In such a case all the crossings of i with channels j to n on the one hand, and of j with channels 1 to i on the other hand, are also inaccessible. In the calculation they are ignored by setting the Landau-Zener probabilities to 1, and the reflections are described by $\alpha_i=\beta_j=0$. The probability $P(b)$ is then given by

$$P(b)=\sum_{k=1}^{\infty} I_k\ . \tag{27}$$

---

*Present address: DIP/SPRO, Centre d'Etudes Nucleaires de Fontenay-aux-Roses, 92265 Fontenay-aux-Roses Cédex, France.

[1] J. A. Hornbeck, Phys. Rev. **84**, 615 (1951); J. A. Hornbeck and J. P. Molnar, *ibid.* **84**, 621 (1951).

[2] J. E. Lawler, A. I. Ferguson, J. E. M. Goldsmith, D. J. Jackson, and A. L. Schawlow, in *Laser Spectroscoy IV,* edited by H. Walther and K. W. Rothe (Springer, Berlin, 1979), p. 188.

[3] R. C. Williamson, Phys. Rev. 21, 107 (1923).

[4] F. W. Lampe, in *Ion Molecule Reactions,* edited by J. L. Franklin (Butterworths, London, 1972), Vol. 2, p. 601.

[5] B. Carré, F. Roussel, P. Breger, and G. Spiess, J. Phys. B **14**, 4271 (1981).

[6] V. S. Kushawaha and J. J. Lewenthal, Phys. Rev. A **25**, 346 (1982).

[7] M. Cheret, L. Barbier, W. Lindinger, and R. Deloche, J. Phys. B **15**, 3463 (1982).

[8] A. Pesnelle, S. Runge, D. Sevin, N. Wolffer, and G. Watel, J. Phys. B **14**, 1827 (1981).

[9] H. F. Wellenstein and W. W. Robertson, J. Chem. Phys. **56**, 1077 (1972).

[10] C. B. Collins, B. W. Johnson, and M. J. Shaw, J. Chem. Phys. **57**, 5310 (1972).

[11] J. C. Gauthier, F. Devos, and J. F. Delpech, Phys. Rev. A **14**, 2182 (1976).

[12] (a) B. Dubreuil and A. Catherinot, Phys. Rev. A **21**, 188 (1980); (b) A. Catherinot and B. Dubreuil, *ibid.* **23**, 763 (1981).

[13] A.Hitachi, C. Davies, T. A. King, S. Kubota, and T. Doke, Phys. Rev. A 22, 856 (1980).

[14] G. Ringer and W. R. Gentry, J. Chem. Phys. **71**, 1902 (1979).

[15] S. E. Nielsen and R. S. Berry, Phys. Rev. A **4**, 865 (1971).

[16] F. Koike and H. Nakamura, J. Phys. Soc. Jpn. **33**, 1426 (1972).

[17] J. S. Cohen, Phys. Rev. A **13**, 86 (1976); **13**, 99 (1976).

[18] R. S. Mulliken, Phys. Rev. **136**, A962 (1964).

[19] S. E. Nielsen and J. S. Dahler, J. Chem. Phys. **71**, 1910 (1979).

[20] (a) A. Pesnelle, S. Runge, M. Perdrix, D. Sevin, and G. Watel, J. Phys. B **16**, L193 (1983); (b) A. Pesnelle and S. Runge, in *Invited Papers of the XIII International Conference on the Physics of Electronic and Atomic Collisions, Berlin, 1983,* edited by J. Eichler, I. V. Hertel, and N. Stolterfoht (North-Holland, Amsterdam, 1984), p. 559.

[21] S. Runge, A. Pesnelle, M. Perdrix, D. Sevin, N. Wolffer, and G. Watel, Opt. Commun. **42**, 45 (1982).

[22] J. Fort, J. J. Laucagne, A. Pesnelle, and G. Watel, Phys. Rev. A **14**, 658 (1976).

[23] W. J. Steets and N. F. Lane, Phys. Rev. A **11**, 1994 (1975).

[24] S. L. Guberman and W. A. Goddard III, Phys. Rev. A **12**, 1203 (1975).

[25] S. Runge, Chem. Phys. Lett. **101**, 167 (1983).

[26] S. Runge, Thèse d'Etat, Université de Paris—Sud, Orsay, 1984; S. Runge and A. Pesnelle, in Conferences Invitées du Dixiéme Colloque sur la Physique des Collisions Atomiques et Eletroniques, Aussois, 1984, edited by N. Sadeghi and J. Berlande (unpublished).

[27] A. Dorelon *et al.* (private communication).

[28] E. C. G. Stueckelberg, Helv. Phys. Acta. **5**, 369 (1932).

[29] J. G. Maas, N. P. F. B. van Asselt, P. J. C. M. Nowak, J. Los, S. D. Peyerimhoff, and R. J. Buenker, Chem. Phys. **17**, 217 (1976).

[30] P. Valiron, R. Gayet, R. McCarroll, F. Masnou-Seeuws, and M. Philippe, J. Phys. B **12**, 53 (1979); G. Peach, Comments At. Mol. Phys. **11**, 101 (1982); J. Pascale, Phys. Rev. A **28**, 632 (1983).